Nanoscale nonlinear radio frequency properties of bulk Nb: Origins of extrinsic nonlinear effects

Tamin Tai,[1,2,*] B. G. Ghamsari,[2] T. Bieler,[3] and Steven M. Anlage[1,2]

[1]*Department of Electrical and Computer Engineering, University of Maryland, College Park, Maryland 20742-3285, USA*

[2]*Department of Physics, Center for Nanophysics and Advanced Materials, University of Maryland, College Park, Maryland 20742-4111, USA*

[3]*Chemical Engineering and Materials Science, Michigan State University, East Lansing, Michigan 48824, USA*

(Received 15 July 2015; published 16 October 2015)

The performance of niobium-based superconducting radio frequency (SRF) particle-accelerator cavities can be sensitive to localized defects that give rise to quenches at high accelerating gradients. In order to identify these material defects on bulk Nb surfaces at their operating frequency and temperature, a wide-bandwidth microwave microscope with localized and strong RF magnetic fields is developed by integrating a magnetic write head into the near-field microwave microscope to enable mapping of the local electrodynamic response in the multi-GHz frequency regime at cryogenic temperatures. This magnetic writer demonstrates a localized and strong RF magnetic field on bulk Nb surface with $B_{\text{surface}} > 10^2$ mT and submicron resolution. By measuring the nonlinear response of the superconductor, nonlinearity coming from the nanoscale weak-link Josephson junctions due to the contaminated surface in the cavity-fabrication process is demonstrated.

DOI: 10.1103/PhysRevB.92.134513 PACS number(s): 74.70.−b, 07.79.−v, 74.25.N−, 74.50.+r

I. INTRODUCTION

There is continued interest in building high-energy accelerators to bring electrons and positrons up to near-light velocity using bulk niobium (Nb) superconducting radio frequency (RF) cavities [1]. These electromagnetic cavities resonate at microwave frequencies and can efficiently transfer microwave power into the kinetic energy of the charged particle beam [2,3]. Each cavity operates with regions of high electric and magnetic RF fields, with the highest electric field on the accelerating axis and maximum magnetic field on the equator surface of the cavity [3]. However, to put these laboratory-fabricated cavities into commercial mass production, many issues arise. It is a challenge to manufacture such high-performance cavities with a high degree of consistency. Much debate regarding this inconsistent performance concluded that certain types of defects on the Nb cavity surface can behave as a source of quenching in tangential high-RF magnetic fields [4–6]. A quench is when the Nb superconductor returns to the normal state in the presence of strong fields, thus limiting their utility. Candidates for these defects include pits, oxides, hydrides, impurity inclusions, grain boundaries, etc. [7,8]. These defects arise from cavity-fabrication steps such as forming, machining, electron-beam welding, electropolishing (EP), and buffered chemical polishing (BCP). These defects are either nonsuperconducting or have lower T_c (for example, NbO_x with $x \sim 0.02$–0.04 has T_c ranging from 5.1 to 6 K [9]), making them sources of dissipation and interrupting the superconducting current flow. Unfortunately, it is difficult to totally remove all of these defects even after sophisticated physical and chemical treatments. Because different defects have their individual quench limit, not all of the defects behave as sources of quenching in certain operating conditions (for example, a 9-cell Tesla cavity usually operates at a temperature of 2 K, an initial accelerating gradient of 25 MV/m, 1.3 GHz RF frequency, and 10 MW pulsed klystron power [3]). Unfortunately, it is not known which defects have lower quench limits and therefore it is necessary to quantitatively understand each type of defect.

Due to the defect issues with Nb, ideally one would like a microscopic technique that identifies defects based on their poor microwave performance at low temperatures in the superconductive state. Quenches often occur in regions of the cavity with strong tangential magnetic field, hence a local probe with strong RF magnetic field concentration is desired. Generally speaking, creating a concentrated microwave magnetic field in a small area of the sample is a challenge and has created interest among several research groups using different methods. Figure 1 shows a brief summary of developments of localized high-RF magnetic field measurements. Our objective is to move into the upper-left quadrant of this diagram or, in other words, to develop a microscopic probe that simultaneously produces a very strong RF magnetic field over a very limited area of the sample. The conventional method is to make a loop-shaped coil as small as possible to generate a strong magnetic field on the sample [10–14]. Some groups also bundle many loop-shaped coils to generate a strong localized field [15], but unfortunately this method sacrifices spatial resolution. Recently, several groups have used the method of either photolithography or electron-beam lithography to fabricate a microcoil and have successfully generated about 10 to 50 Tesla of pulsed magnetic field on 30 ns time scales [16,17]. One group also demonstrated that this nanosecond pulsed field can switch the magnetization of nanomagnetic particles [18], but this method will generate heat and may not be useful to probe the properties of superconductors due to the complicated sample heating during the measurement. Another study of utilizing spin-torque-driven microwaves to generate a localized RF magnetic field to flip the magnetization direction of a thin single-domain magnetic element has been widely discussed recently [19–23]. However, this technique does not have application yet in investigating the properties of superconducting radio frequency (SRF) cavities.

In the microwave microscope approach described here, a magnetic write head from a hard-disk drive is used as a near-field scanning probe to generate a strong and localized RF field on a superconducting sample [24–29]. The device

*tamintai@gmail.com

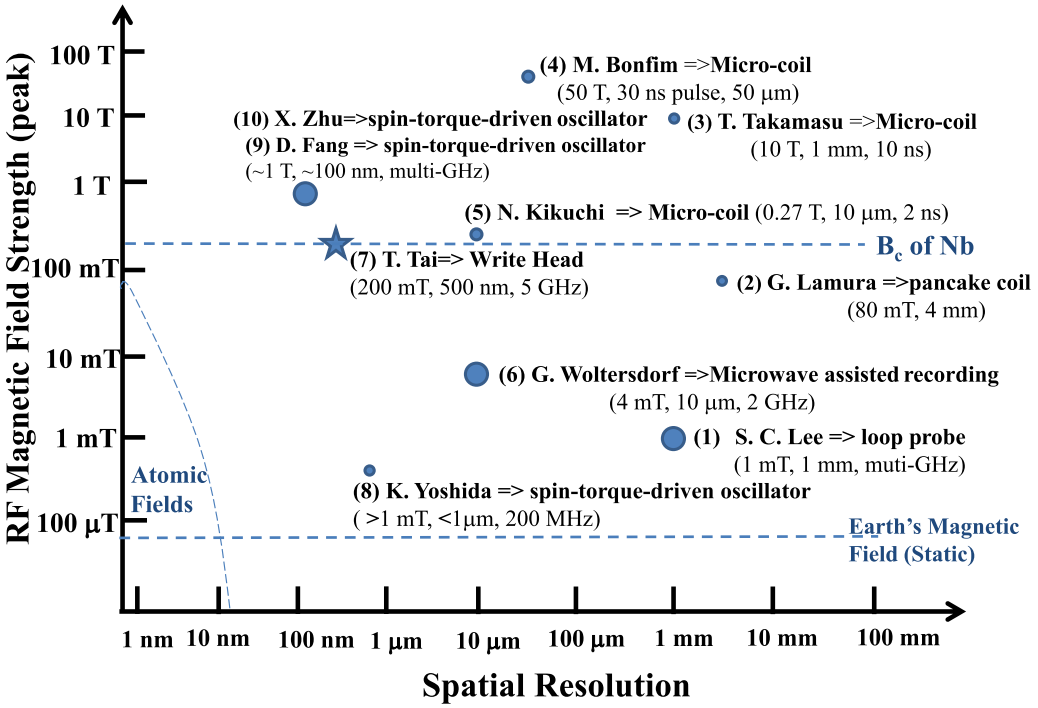

FIG. 1. (Color online) High-field, high-resolution ac/transient magnetic microscopy generating highly confined magnetic fields with frequency $\geqslant$100 MHz: A selected summary of methods to generate a highly concentrated RF magnetic field. Each technique lists a typical RF magnetic field scale, degree of spatial confinement/resolution, and demonstrates an associated time/frequency scale. All of the candidate technologies are numbered and referenced as follows: (1) Lee: loop probe [10–12]; (2) Lamura: pancake coil [15]; (3) Takamasu: microcoil [16]; (4) Bonfim: microcoil [17]; (5) Kikuchi: microcoil [18]; (6) Woltersdorf: microwave-assisted recording [19]; (7) Tai: magnetic write head [26,28]; (8) Yoshida: spin-torque-driven oscillator [20]; (9) Fang: spin-torque-driven oscillator [21]; (10) Zhu: spin-torque-driven oscillator [22]. Note that the larger circle (●) and star sign (★) indicate the operation frequency/speed that corresponds to higher frequencies. The star sign also indicates the method used in this paper.

is a high-resolution magnetic microscope probe in the GHz frequency regime. The superconducting sample responds by creating screening currents to maintain the Meissner state in the material. These currents inevitably produce a time-dependent variation in the local value of the superfluid density, and this in turn generates a response at harmonics of the driving tone. At localized defective regions, which will cause premature quench of the cavity, the enhanced harmonic response will be more significant.

The nonlinear third-harmonic response frequency is studied in this paper because that one is intrinsically always present (to a greater or lesser extent) in a superconductor in the zero dc field at finite temperature. In addition to this intrinsic response, extrinsic properties (i.e., associated with defects) generate their own third-harmonic response, almost always at a level far stronger than the intrinsic response [30]. Figure 2(a) illustrates a schematic situation in which defects stimulated by a localized scanned RF magnetic field probe show enhanced nonlinear response compared to the background intrinsic response. One can parametrize the nonlinear response with an associated "nonlinear critical current density" called J_{NL}. The nonlinearity is quantified in terms of the effect that the defect has on the superfluid density n_s with increasing RF current J. This is written as $\frac{n_s(T,J)}{n_s(T,0)} \cong 1-(\frac{J}{J_{NL}})^2$, showing that regions with small J_{NL} will have enhanced suppression of the superfluid density [10–12,31]. The values of J_{NL} associated with the intrinsic Nb background material, and several defects, are also shown schematically in Fig. 2(b). The third-harmonic power is inversely proportional to J_{NL} as $P_{3f} \sim (\frac{1}{J_{NL}})^4$ in thin-film superconductors [10–12]. Hence defective regions with smaller J_{NL} will produce larger harmonic power (P_{3f}), revealing their presence in the scanned probe microscope. Note that a number of papers have reported quantitative measurement and imaging of J_{NL} values, mainly in high-temperature superconductors. Several papers have determined

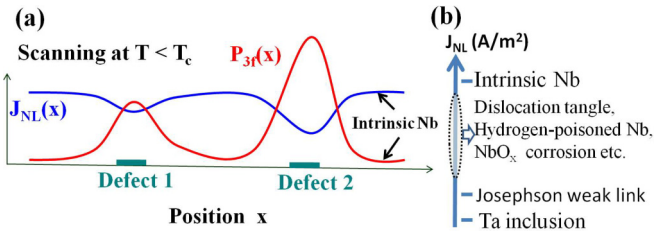

FIG. 2. (Color online) (a) Schematic J_{NL} variation on the superconducting surface from intrinsic Nb to different discrete defects. The P_{3f} generation from defects is local. The defects with greatest disruption of the superfluid density have the lowest J_{NL} and strongest P_{3f}. Hence, measuring P_{3f} at different positions can be used to find defects on superconductors. (b) A speculative schematic hierarchy of a few representative defects and their associated J_{NL} values. The dashed oval region indicates the unknown order of the J_{NL} hierarchy for these types of defects.

values associated with bicrystal grain boundaries [10–12] and measured one-dimensional line cuts of $J_{NL}(x)$, similar to Fig. 2(a). Other work has determined J_{NL} for weak links [31,32] in cuprate superconductors.

This paper will first address experimental measurements (Secs. II and III) of the nonlinear third-harmonic response from bulk Nb materials in localized regions down to submicron-length scales. In Sec. IV, a detailed discussion of the quantitative modeling of the experimental results will be given; Sec. V contains the conclusion. This paper provides a more detailed examination of the preliminary data presented in Ref. [28].

II. EXPERIMENT

A bulk Nb sample with T_c of 9.2 K and well-defined locations of defects is an ideal candidate for measurement of nonlinearity using a microwave microscope. Figure 3(a) shows a schematic diagram of the original tensile specimen made from bulk Nb with a high residual-resistivity ratio (RRR). The surface of three tensile specimens was mechanically polished and then electropolished prior to deformation. To simulate an elliptical SRF cavity forming a welding process using large-grain niobium, single-crystal samples were strained to 40% elongation, cut in half, and then different halves were welded together. Figure 3(b) shows the finished specimen. The sample has been carefully imaged by electron backscattered pattern (EBSP) orientation imaging microscopy (OIM) [33] and a variety of microstructural conditions have been identified, including as-deformed regions that were kept cold near the end, recrystallized regions with several grain boundaries in the center, and recovered regions in between, with many niobium oxides, grain boundaries, and dislocations on the surface. The

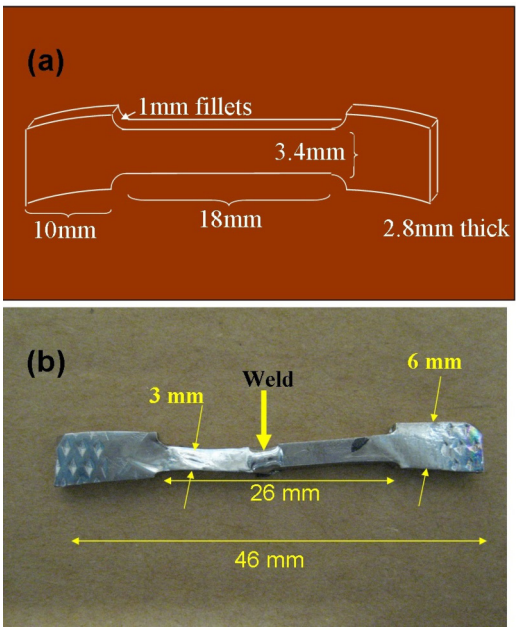

FIG. 3. (Color online) (a) A schematic picture of the bulk Nb tensile specimen before deformation. All dimensions of the specimen are labeled. (b) The finished specimen after tensile test and welding treatment in the center of the sample.

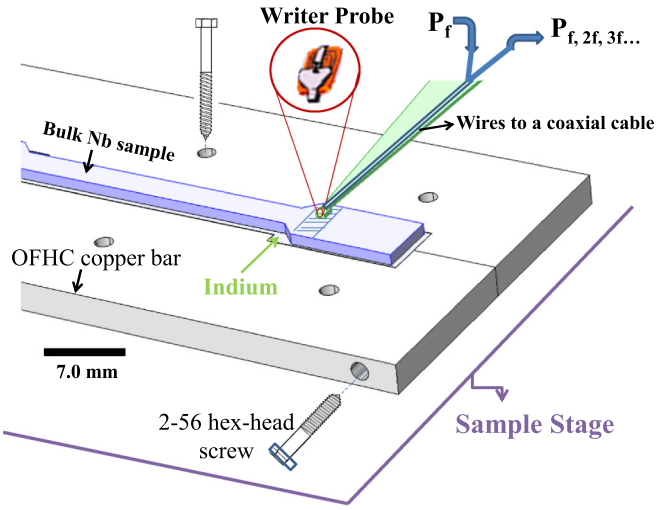

FIG. 4. (Color online) The setup inside the cryostat probe station for measuring the bulk Nb nonlinearity. The slashed region on the top of the bulk Nb sample indicates where the P_{3f} measurements are performed. The circled zoomed-in picture schematically highlights the magnetic write-head probe on the surface of the bulk Nb. Note that thermal anchoring is critical for cooling the bulk Nb sample below T_c.

OIM analysis identified several specific defects that appear in the processing of bulk Nb cavities.

In order to make the sample surface superconducting in our microscope cryostat system, thermally anchoring the sample and good radiation shielding from the outside environment are crucial. Figure 4 shows the setup inside the cryostat. The bulk Nb sample is clamped in place by two halves of an oxygen-free high-conductivity (OFHC) copper bar. Indium is filled within the gap between the Nb sample and OFHC copper bar to reduce the thermal resistance between bulk Nb and the OFHC copper bar. The two halves of the bar are bolted together laterally by two 2-56 hex-head screws from the side and then the whole OFHC copper bar assembly is bolted directly onto the surface of the sample stage in the cryostat, with vacuum grease in between to reduce the thermal resistance. Note that the sample stage is also made of OFHC copper and is also firmly bolted on the top of the cold plate. A thermometer is placed on the bulk Nb top surface to monitor the temperature of the relevant surface of the sample. An OFHC copper cryogenic radiation shield is attached to the cold head of the cryostat. The lid of the radiation shield has a 3-inch-diameter infrared blocking window as a view port. This setup can cool down the bulk Nb sample top surface to 5.0 K without pumping the exhaust from the cryostat. By pumping the exhaust, the surface temperature of the bulk Nb can go below 4.0 K. However, 5.0 K is cold enough to analyze the surface microwave properties of this bulk Nb sample. Note that if these extensive precautions are not taken, it is virtually impossible to cool the surface of bulk Nb down below its transition temperature. More photos inside the vacuum chamber can be found in Ref. [34].

The principles of measuring the complex third-harmonic voltage (V_{3f}^{sample}) or related scalar power (P_{3f}^{sample}) that are generated by the sample due to local excitation at a fundamental frequency from the magnetic write head have been widely discussed in previous publications [24–26,28]. The

magnetic write head is made by Seagate (part no. GT5) and was originally designed for longitudinal magnetic recording. Hence it creates a strong tangential RF magnetic field on the surface of the sample. The superconducting sample in proximity to the probe responds by creating screening currents to maintain the Meissner state in the material. These currents inevitably produce a time-dependent variation in the local value of the superfluid density, and this in turn generates a response at harmonics of the driving tone. A high pass filter is used outside the cryostat to suppress the reflected $P_{f,2f}$ and pick up the P_{3f} signal.

III. THIRD-HARMONIC MEASUREMENT RESULTS ON BULK Nb

Many localized third-harmonic measurements are performed in the slashed region indicated in Fig. 4. Based on OIM analysis, this region has a moderately high density of disorganized dislocations due to thermal stresses from ingot cooling, and some plastic deformation from the tensile test. The probe height is determined by optical microscopy from the side of the cryostat combined with $S_{11}(f)$ measurement of the magnetic write head to decide the best excitation frequency. The probe height is approximately within 1 μm from the bulk Nb surface. The details of the probe height control are discussed in Refs. [27,34]. Different locations show slightly different microwave nonlinear properties and will be illustrated qualitatively in this section.

Figure 5 shows one of the representative measurements for the power dependence of P_{3f} with respect to fundamental input power P_f at two fixed temperatures (above T_c and below T_c) under 5.025 GHz excitation at this area. The representative curve measured at $T = 8.7$ K (below T_c) shows a distinct P_{3f} onset from the noise floor of the spectrum analyzer followed by a continuous increase of nonlinearity until a turnover occurs at high excitation power. Then the $P_{3f}(P_f)$ data at high excitation power eventually approach and oscillate around the probe background nonlinearity, $P_{3f}^{\text{probe}}(P_f)$, measured at $T = 20$ K. First, the onset of the

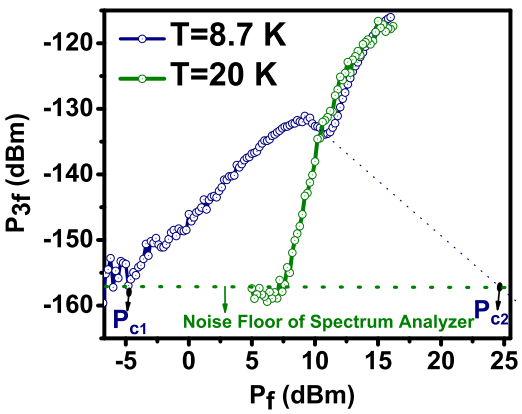

FIG. 5. (Color online) The P_{3f} dependence on P_f at a selected temperature of 8.7 K for local microwave excitation of bulk Nb with the magnetic write-head probe. Note that the T_c of the bulk Nb sample is 9.2 K. The P_{3f} at $T = 20$ K results from the probe nonlinearity itself.

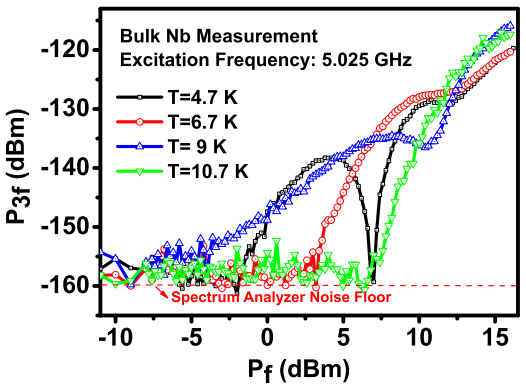

FIG. 6. (Color online) The P_{3f} dependence on P_f at selected temperatures on the bulk Nb sample with the magnetic write-head probe. The P_{3f} dependence on P_f at 4.7 K shows a different nonlinear behavior compared to the other two temperatures. The nonlinearity of the probe is measured at $T = 10.7$ K in this data set.

nonlinear response can be defined as a temperature-dependent lower critical power, P_{c1}. This onset power P_{c1} will shift toward larger excitation power at lower temperature on the Nb superconductor (Fig. 6) [28]. In addition, after a turnover, all $P_{3f}(P_f)$ curves tend to decrease with increasing power, suggesting that Nb superconductivity is suppressed. The linear extrapolation of P_{3f} to the noise floor of the spectrum analyzer can be defined as an upper critical power P_{c2}, which suggests that superconductivity will eventually be destroyed due to the high-RF magnetic field. It is seen that higher P_{c2} is required to destroy the superconductivity at lower temperature [28]. The temperature-dependent P_{c1} and P_{c2} can be associated with temperature-dependent surface field B_{c1} and B_{c2} (or perhaps B_c). The analysis of the temperature-dependent P_{c2} has been used to estimate the surface field excited by the magnetic write-head probe. This analysis has been carried out by a fit of the experimental temperature-dependent critical field $B_c(T)$ from each experimental P_{c2} with the approximate equation $B_c(T) \cong B_c(0\text{ K})[1-(T/T_c)^2]$, valid near T_c [28]. The fit indicates that localized magnetic field from the magnetic write-head probe is of the order of the thermodynamic critical field of Nb with $B_{\text{surface}} \sim 10^2$ mT [28]. Different positions will show different P_{c1} and P_{c2} values due to the inhomogeneity of the bulk Nb surface properties.

If the inhomogeneity of the Nb surface contains Nb hydride or Nb oxide, which have lower critical temperature, then a weak-link Josephson junction may form there. In this case, the curve of P_{3f} versus P_f will behave differently from the case of the homogeneous bulk. Figure 6 shows the P_{3f} versus P_f at 4.7 K compared to that at $T = 9$ and $T = 6.7$ K. One can see that at $T = 4.7$ K, the curve of P_{3f} versus P_f shows an additional peak while the excitation power is between -2.5 and 7 dBm. This implies that some additional source of nonlinearity is excited at this temperature. A detailed interpretation will be given in Sec. IV.

The temperature dependence of $P_{3f}(T)$ at the same probe position is shown in Fig. 7 at two values of P_f. The onset of Nb nonlinearity begins immediately at the bulk Nb T_c (9.2 K) and then quickly saturates before $T = 8$ K for $P_f = 5.5$ dBm, 5.025 GHz excitation. The nonlinearity shows a dip around

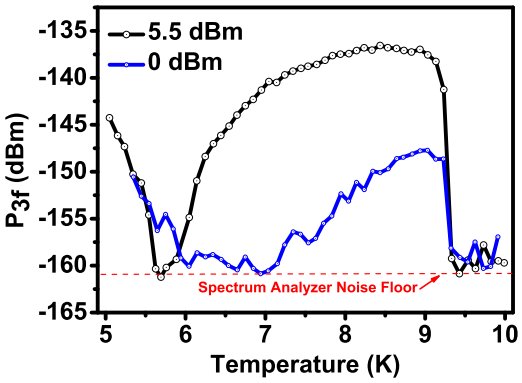

FIG. 7. (Color online) The temperature-dependent $P_{3f}(T)$ (measured as temperature decreases) of the bulk Nb sample at two specific input powers and 5.025 GHz excitation. Note that the T_c of the bulk Nb sample is 9.2 K and the onset of nonlinearity at low excitation power also begins at exactly 9.2 K.

5.8 K. Below 5.8 K, the nonlinearity increases again. This same qualitative behavior also happens at a lower excitation power of $P_f = 0$ dBm. From this temperature-dependent nonlinear behavior, the measured response at high power is consistent with the nonlinearity from the Josephson effect [35,36]. This situation will happen on the bulk Nb surface due to the presence of oxides and hydrides forming weak-link Josephson junctions [37,38], for example. In the next section, the nonlinear mechanisms active in the bulk Nb measurement are modeled by the weak-link Josephson nonlinear effect.

IV. MODELING NONLINEARITY

Possible extrinsic nonlinear mechanisms for the bulk Nb measurements include moving vortices [39] and the weak-link Josephson effect [35,36]. The data presented in Sec. III can be reasonably well explained by the nonlinear electrodynamics of the bulk Nb superconductor suffering phase slips [40] across a Josephson junction [36]. Josephson junctions will form on the inner surface of the bulk Nb cavities due to the inevitable oxidation in air [38] and exposure to water vapor. This surface oxidation deteriorates the superconductivity because of the formation of superconductor-insulator-superconductor (S-I-S), superconductor–normal-metal–superconductor (S-N-S), or superconductor-constriction-superconductor (S-C-S) structures [37]. In addition, Josephson junctions may also develop on the Nb surface due to the chemical surface treatment during fabrication.

To model the weak-link Josephson nonlinearity, we consider a perpendicular magnetic field component that induces a single screening current loop passing through N identical defects, which are arrangements of dislocations, dislocation tangles, or impurities as shown schematically in Fig. 8. These subgrains are weakly connected together in a closed loop of area S. This loop can be driven by a combined dc field (B_{dc}) and RF field (B_{rf}) on the superconducting surface, giving rise to a total flux of

$$\Phi(t) = \Phi_{dc} + \Phi_{rf}\sin(\omega t),$$
$$\text{with} \quad \Phi_{dc} = \frac{SB_{dc}}{\Phi_0} \quad \text{and} \quad \Phi_{rf} = \frac{SB_{rf}}{\Phi_0}, \qquad (1)$$

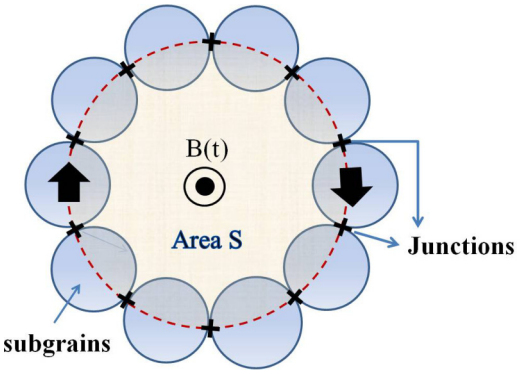

FIG. 8. (Color online) Schematic illustration of an induced screening current loop created by the magnetic field pointing out of the paper. Multiple defects such as subgrains are connected by weak-link Josephson junctions between the defects. Note that S is the area of the screening current loop. The arrow directions illustrate the direction of the diamagnetic current. This figure indicates ten Josephson junctions.

where $\Phi(t)$ is the total normalized magnetic flux through the loop, in units of the flux quantum Φ_0, and Φ_{dc} is the normalized dc flux. Φ_{rf} and B_{rf} are the normalized flux and amplitude of the normal-surface RF field, respectively. In this experiment, Φ_{dc} is assumed to be zero because there is no applied dc field and we assume that there is no stray dc field from the write head or the environment.

A loop of N defects under the applied RF magnetic flux (Φ_{rf}) will have an internal energy (E), which can be defined by the Josephson coupling Hamiltonian [36]. Clearly, if Φ_{rf} is higher than the cusp of Josephson coupling energy (either higher than the first, second, or even higher energy cusp), a phase slip will occur in the junction [36]. Hence, for the amplitude of RF flux shown in Fig. 9, a phase slip will occur at four times in the first half of the RF cycle: at times t_1, t_2, t_3, and t_4, where t_1 and t_4 are the times when the applied magnetic

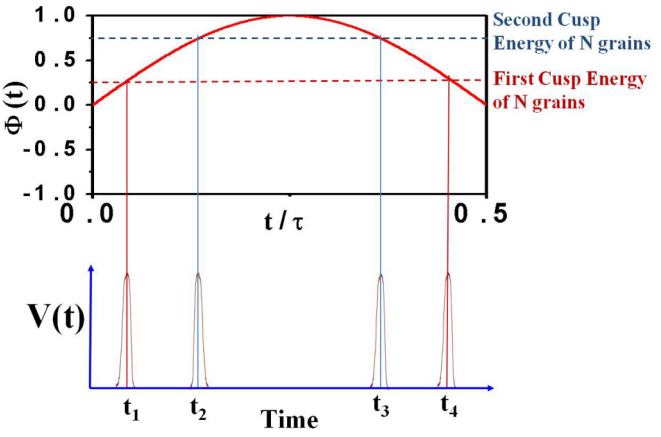

FIG. 9. (Color online) Upper frame: Normalized magnetic flux without the presence of dc field [$\Phi(t) = \Phi_{rf}\sin(\omega t)$]. This figure assumes the cusps of the energy appear when $\Phi = 0.25$ and 0.75. Lower frame: The generated voltage spikes in a half RF cycle (τ) due to the presence of phase slips of Josephson junctions in the loop of N subgrains.

flux is equivalent to the first cusp of the energy of the N grain junction ring and t_2 and t_3 are the times when the applied magnetic flux is equivalent to the second cusp of the energy of the N grains.

The response voltage due to the phase slip of the Josephson junction is given by

$$V(t) = -\frac{\hbar}{2e}\frac{d\phi}{dt}, \tag{2}$$

where ϕ is the gauge-invariant phase difference across a Josephson junction. This voltage is a series of four spikes in each half RF period, corresponding to each of the four phase-slip events. We project out the third-harmonic voltage by making a sine and cosine expansion in the harmonics of the fundamental drive frequency,

$$\begin{aligned} V_{3fa} &= \frac{2}{\tau}\int_0^\tau V(t)\sin(3\omega t)dt, \\ V_{3fb} &= \frac{2}{\tau}\int_0^\tau V(t)\cos(3\omega t)dt, \end{aligned} \tag{3}$$

where τ is the RF period. This yields the following expression for the third-harmonic voltage for the case of n phase-slip events in each period:

$$\begin{aligned} V_{3fa} &= -\frac{\hbar}{e}\frac{2\pi\omega}{N}\left[\sum_i^n |\sin(3\omega t_i)|\right], \\ V_{3fb} &= -\frac{\hbar}{e}\frac{2\pi\omega}{N}\left[\sum_i^n |\cos(3\omega t_i)|\right], \end{aligned} \tag{4}$$

where N is the number of equivalent Josephson junctions in the loop.

In the experiment, the current loop couples flux back to the magnetic write-head probe. Hence what we measure is an induced voltage in the magnetic write-head probe given by $V_e = d\Phi_e/dt$, where Φ_e is the time-dependent induced flux at the write-head probe. To estimate the voltage induced on the magnetic probe, one can consider a magnetic dipole moment over the superconductor at a distance a from the superconducting surface [41–44], as shown in Fig. 10. The magnetic dipole can be described by a Dirac delta function, $\mathbf{M}\delta(x)\delta(y)\delta(z-a)$, where $\mathbf{M}$ is the moment of the dipole. The superconductor maintains itself in the Meissner state and generates a screening current on the superconducting surface. The radial and azimuth-angle components of the generated screening current due to this dipole can be expressed as [44]

$$\begin{aligned} J_\rho(\rho,\theta) &= -\frac{M\sin\theta}{4\pi\lambda^2}\frac{\sqrt{\rho^2+a^2}-a}{\rho^2\sqrt{\rho^2+a^2}}, \\ J_\theta(\rho,\theta) &= \frac{M\cos\theta}{4\pi\lambda^2}\left[\frac{\sqrt{\rho^2+a^2}-a}{\rho^2\sqrt{\rho^2+a^2}} - \frac{a}{(\rho^2+a^2)^{3/2}}\right], \end{aligned} \tag{5}$$

where ρ and θ indicate the radial distance and the azimuth angle with respect to an origin on the surface just below the dipole (see Fig. 10). Hence, the maximum current $J_{\max}$ induced by a magnetic dipole moment M at a height a above the superconductor with penetration depth λ will be at the location

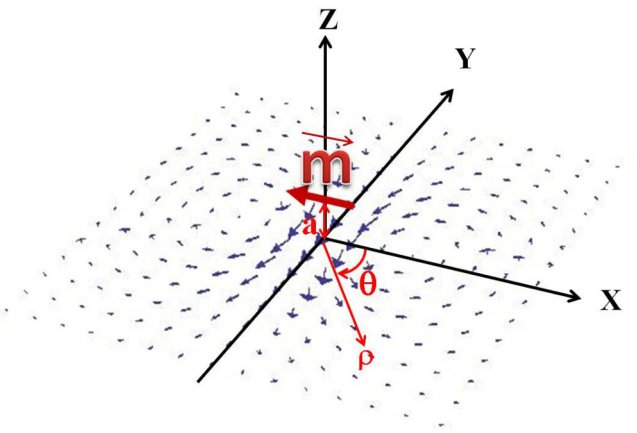

FIG. 10. (Color online) The screening current (J) induced in a superconductor due to a point magnetic dipole $\vec{m}$ with a distance a above the superconducting surface plane ($Z = a$). ρ and θ are the radial distance and azimuth angle, respectively. Surface current calculation from Ref. [44].

of $\rho = 0$ and $\theta = -\pi/2$,

$$\begin{aligned} J_{\max} \equiv J_\rho(\rho=0,\theta=-\pi/2) &= \frac{M}{8\pi\lambda^2 a^2}, \\ J_\theta(\rho=0,\theta=-\pi/2) &= 0. \end{aligned} \tag{6}$$

The magnetic dipole moment M also can be expressed in terms of the magnetic flux in the gap of the probe as $M = \Phi_e l_{\text{gap}}/\mu_0$, where l_{gap} is the length of the magnetic gap on the bottom of the magnetic yoke [27]. Hence the induced voltage on the probe can be written as

$$V_e = \frac{d\Phi_e}{dt} = \frac{d}{dt}\frac{\mu_0 M}{l_{\text{gap}}} = \frac{dJ}{dt}\frac{8\pi\mu_0\lambda^2 a^2}{l_{\text{gap}}}. \tag{7}$$

Take an estimate of the third-harmonic current density to be $J_3 = I_3/(\lambda a)$, where I_3 is the third-order harmonic current, and, in combination with Eq. (4), the induced third-harmonic voltage for sine and cosine expansion and the corresponding third-harmonic power generated by this phase-slip mechanism in the weak-link Josephson junction are given in the frequency domain by

$$\begin{aligned} V^e_{3fa} &= \frac{96\mu_0\omega\lambda(T)aI_3(T)}{Nl_{\text{gap}}}\left[\sum_i^n |\sin(3\omega t_i)|\right], \\ V^e_{3fb} &= \frac{96\mu_0\omega\lambda(T)aI_3(T)}{Nl_{\text{gap}}}\left[\sum_i^n |\cos(3\omega t_i)|\right], \\ P_{3f} &= \frac{\sqrt{\left(V^e_{3fa}\right)^2+\left(V^e_{3fb}\right)^2}}{2Z_0}, \end{aligned} \tag{8}$$

where $Z_0 = 50\Omega$, the characteristic impedance of the microwave generator. A complete calculation of the temperature- and power-dependent I_3 has been carried out in Ref. [35]. The outcome shows that $I_3 = I_c(T)J_3(\beta)\sin(3\omega t)$, with $\beta \equiv \frac{2\pi SB_{rf}}{\Phi_0}$ coming from the third-order expansion of the Fourier series for $I(t) = I_c\sin[\beta\sin(3\omega t)]$ in terms of the Bessel function $J_n(\beta)$ [35]. Here, I_c is the junction critical current, which

we take to be the Ambegaokar and Baratoff estimation [40,45],

$$I_c(T) = \frac{\pi \Delta(T)}{2eR_n} \tanh\left[\frac{\Delta(T)}{2k_B T}\right], \quad (9)$$

where $\Delta(T)$ is the temperature-dependent superconducting gap parameter and R_n is the normal resistance of the junction. The temperature dependence of $\lambda(T)$ can be calculated according to BCS theory with the zero-temperature London penetration depth of Nb $\lambda_0 = 40$ nm [46].

To simplify the calculation for fitting experimental $P_{3f}(P_f)$ and $P_{3f}(T)$ data, the number of Josephson junctions N as shown in Fig. 8 in the current loop is assumed to be ten in Eq. (8). This assumption is based on Halbritter's estimation that weak links on the surface of bulk Nb are ~10–100 nm apart [9,47]. In addition, both square-bracketed terms in Eq. (8) are assumed to be of the order of one. The distance between the probe and sample, a, is assumed to be 100 nm, which is the scale of the magnetic gap and flying height during the reading and writing process in high-speed magnetic recording [48,49]. Two parameters, R_n and β, are left for fitting.

From the power-dependence measurement shown in Figs. 5 and 6, one can see that the probe nonlinearity P_{3f}^{probe} participates in the measurement at high excitation power. In order to extract the response from only the superconducting sample at high power, an effective P_{3f} is defined by taking the absolute value of the difference between the measured P_{3f} in the superconducting state and the measured P_{3f} in the normal state, without considering the relative phases of the contributing nonlinearity. This crude subtraction process provides a qualitative measure of the high-power nonlinear response of the sample. Therefore, the effective P_{3f} can be regarded as the nonlinearity arising from just the superconducting sample, to a first approximation.

The points in Fig. 11 show the effective P_{3f} at the representative temperature of 9 K from the experimental data in Fig. 6. The solid line in Fig. 11 indicates the fit to the phase-slip model for the temperature of $T = 9.0$ K. The relation between

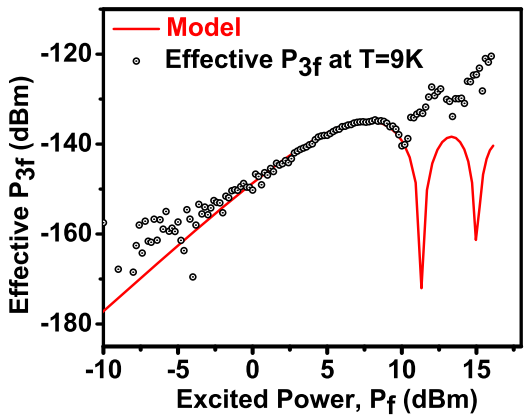

FIG. 11. (Color online) Effective P_{3f} vs P_f for the bulk Nb sample measured by the magnetic write-head probe at 9 K under 5.025 GHz excitation, as shown by the dot points. The solid line is the theoretical calculation based on the phase-slip model of the Josephson junction. The parameters are as follows: $T = 9.0$ K, frequency = 5.025 GHz, $R_n = 90\ \Omega$, $S = 9.11 \times 10^{-14}\text{m}^2$, $a = 100$ nm, $N = 10$, $l_{\text{gap}} = 100$ nm. Only R_n and S were varied to perform the fit.

the incident fundamental power P_f and the actual surface magnetic field experienced on the bulk Nb surface is taken as $P_f = k{B_{rf}}^2$ with $k = 25.6\text{W/T}^2$ [28] directly for fitting the effective P_{3f}, where B_{rf} is the amplitude of the surface magnetic field on the bulk Nb superconductor and k is a coupling coefficient between the probe and sample to connect the power and magnetic field. The value of k can be judged by the field scale generated by a finite-element simulator and experimental results on a known conventional superconductor for calibration [28]. Again, the fits assume constant values of the probe height $a = 100$ nm, the number of Josephson junctions $N = 10$, and the magnetic gap of the yoke $l_{\text{gap}} = 100$ nm. Then only the product of SB_{rf} (which comes from the definition of $\beta \equiv \frac{2\pi SB_{rf}}{\Phi_0}$) and R_n will affect the calculated P_{3f}.

Finally, two parameters, R_n and S, are varied to fit the model [Eq. (8)] to the data. Varying R_n can adjust the amplitude of P_{3f}, and varying S can laterally shift the theoretical curve to locate the first $P_{3f}(P_f)$ dip position in the experimental data. From Fig. 11, the dip position of the model at $P_f = 11.3$ and $P_f = 15.0$ dBm is matched to the dip position of the effective P_{3f} measurement taken at 9 K under 5.025 GHz excitation by taking $S = (302\text{ nm})^2$. However, the model shows deep dips but the experimental data does not. It is clear in Fig. 6 that the data of P_{3f} at $T < T_c$ intersect with the $P_{3f}^{\text{probe}}(T = 10.7\text{ K})$ (background level) at high excitation power, implying deep minima in the harmonic response of the superconductor. The crude background-subtraction method from limited data points obscures these minima. The amplitude of P_{3f} at the first peak is matched to the model by taking $R_n = 90\Omega$. This junction resistance is consistent with Halbritter's estimation for a bulk Nb weak-link junction, which is $R_{bl} \approx 10^{-15}\ \Omega\,\text{m}^2$ [47,50]. At higher power, the amplitude of the effective P_{3f} does not match the phase-slip theoretical curve after the first dip. Several issues may be at play: first, when the applied field is higher than the vortex nucleation field, the generation, motion, and annihilation of vortices will contribute a significant nonlinear response [39]. In addition, vortices pinned by defects will oscillate with the competition of pinning and image attraction forces, generating harmonic response [39]. This vortex-pinning phenomenon becomes significant at strong fields, which push the vortex deeper past pinning sites. Another reason is that the probe nonlinearity is oversimplified in the calculation: the phase of the V_{3f}^{probe} is not included when subtracting the measured P_{3f} in the normal state from the measured P_{3f} in the superconducting state.

The loop area S for the fit at $T = 9$ K (Fig. 11) is $S = 9.12 \times 10^{-14}\text{ m}^2$, equivalent to a circular loop with radius $r = 170$ nm. This value of the fit loop radius is on the scale of the magnetic gap (~100 nm) in the write-head probe and implies the resolution of the magnetic write-head probe in the near-field microwave microscope. This length scale is also consistent with those put forward by Halbritter for the distance between weak links on the surface of air-exposed bulk Nb [9,37,47,50].

A summary of the temperature-dependent R_n and S from our model fits for the effective P_{3f} at different temperatures is shown in Fig. 12. We see that these two parameters are temperature dependent (note that the number of junctions in the loop, N, could also vary, but here we choose to keep this value fixed). One reason for temperature-dependent

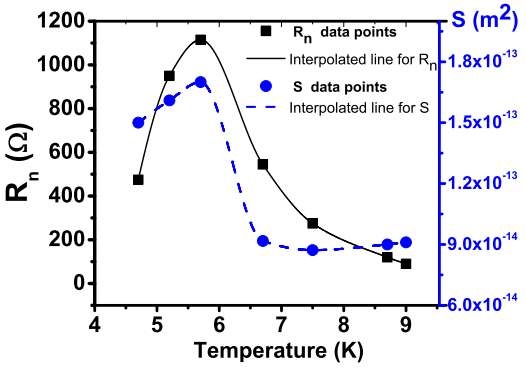

FIG. 12. (Color online) Temperature-dependent fitting parameters R_n (normal resistance of the junction as square symbols) and S (area of the induced screening current loop as circle symbols). Each value is determined by the fitting method of the phase-slip model from the P_{3f} vs P_f data in Fig. 6. Note that all data points for both R_n and S are connected by an interpolation spline function.

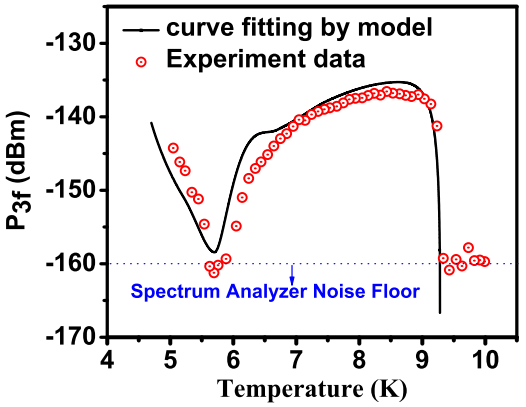

FIG. 13. (Color online) Temperature dependence of the third-harmonic response for the bulk Nb sample at the excitation power 5.5 dBm and excitation frequency 5.025 GHz measured by the magnetic write-head probe (dot points). The noise floor of the spectrum analyzer at this excitation frequency is about −161 dBm. A calculated result (black solid curve) based on the phase-slip model is fit to the data. The fitting parameter is $B_{rf} = 11.75$ mT, with fixed values for the remaining parameters: $l_{\rm gap} = 100$ nm, $N = 10, a = 100$ nm.

R_n and S is because the screening current loop will look for the easiest trajectory with highest critical current of the weak-link Josephson junctions to pass through. One can see that the R_n gradually goes up with decreasing temperature from 9 to 5.7 K. This is consistent with the decrease of quasiparticle density upon going to lower temperature. For $S(T)$, a feature of the jump from low values at $T = 6.3$ K to the larger values at $T = 5.7$ K indicates the loops get bigger at low temperature. The temperature of this jump is coincident with the transition temperature of NbO_x material, or proximity-coupled Nb, in the vicinity of weak links in bulk Nb with reduced transition temperatures of 5.1 to 6.0 K as identified by Halbritter [9]. Below 5.7 K, the $R_n(T)$ decreases with decreasing temperature. This decrease also corresponds to a decrease of the area S with decreasing temperature below 5.7 K. Although we do not know how to interpret this decrease of R_n and S at low temperature, several possible issues may be at play. The localized heating of the sample by the probe may be another possible reason for the nonmonotonic dependence in Fig. 12. These possibilities may affect the screening current area S at low temperature and result in a corresponding change of R_n at low temperature. These results are consistent with the existence of a dense network of weak links on the surface of air-exposed Nb. It is clear that our microscope is probing this complex network on the scale of the defect size and that the network evolves significantly under RF-field excitation as a function of temperature.

Finally, the experimental temperature-dependent $P_{3f}(T)$ with 5.5 dBm excitation in Fig. 7 is also fitted by the phase-slip model. An interpolation function for the temperature dependence $R_n(T)$ and $S(T)$, plotted as the solid line and the dashed line in Fig. 12, respectively, is used for $P_{3f}(T)$ fitting. The black solid line in Fig. 13 is the fit result from the phase-slip model with $B_{rf} = 11.75$ mT. Other parameters ($a = 100$ nm, $N = 10$, $l_{\rm gap} = 100$ nm) remain the same as the fitting of P_{3f} on P_f. The experimental data points are shown in red circles taken at 5.5 dBm excitation power and 5.025 GHz excitation frequency from Fig. 7. Due to the finite number of data points in the interpolation function for the temperature dependence $R_n(T)$ and $S(T)$, the fitting curve shows some discrepancy. However, most of the $P_{3f}(T)$ data points still follow the trend of the phase-slip model. The fit of the 0 dBm data in Fig. 7 is qualitatively correct as well, which makes a compelling case that the nonlinear mechanism comes from the weak-link Josephson junction, while the excitation power is less than the first deep oscillation in the effective $P_{3f}(P_f)$ curve.

V. CONCLUSIONS

A clear reproducible nonlinear response signal from the surface of superconducting bulk Nb is obtained by the magnetic write-head probe. The success of nonlinear excitation on bulk Nb also implies that the magnetic field from the magnetic write-head probe is of the order of the thermodynamic critical field of the measured bulk Nb sample. From fits to the data, nonlinearity from the weak-link Josephson effect can explain the measured nonlinear response on the bulk Nb for both $P_{3f}(T)$ and $P_{3f}(P_f)$ measurements. The measured nonlinearity of the bulk Nb samples is perhaps due to the contaminated surface in the fabrication process or subsequent handling in air. The nonlinear near-field magnetic field microwave microscope has great potential to identify the electrodynamic properties of bulk Nb materials and to image the electrodynamic defects on superconducting Nb in the GHz frequency region. Our work in the measurement of local high-frequency microwave properties of Nb superconductors will help the SRF community understand the key issues that lead to degradation in the performance of Nb cavities.

ACKNOWLEDGMENTS

This work is supported by the US Department of Energy/High Energy Physics through Grant No. DE-SC0012036 and CNAM. The work at Michigan State University was supported by the US Department of Energy-OHEP, Contract No. DE-FG02-09ER41638.

[1] Abdelhak Djouadi, Joseph Lykken, Klaus Mönig, Yasuhiro Okada, Mark Oreglia, Satoru Yamashita *et al.*, International linear collider reference design report, volume 2: Physics at the ILC, arXiv:0709.1893.

[2] H. A. Schwettman, J. P. Turneaure, W. M. Fairbank, T. I. Smith, M. S. McAshan, F. B. Wilson, and E. E. Chamber, Low temperature aspects of a cryogenic accelerator, IEEE Trans. Nucl. Science **14**, 336 (1967).

[3] Hasan Padamsee, Jens Knobloch, and Tomas Hays, *RF Superconductivities on Accelerators*, *Wiley Series in Beam Physics and Accelerator Technology* (Wiley, New York, 1998).

[4] G. Ciovati, G. Myneni, F. Stevie, P. Maheshwari, and D. Griffis, High field Q slope and the baking effect: Review of recent experimental results and new data on Nb heat treatments, Phys. Rev. Spec. Top. - Accel. Beams **13**, 022002 (2010).

[5] Z. H. Sung, A. A. Polyanskii, P. J. Lee, A. Gurevich, and D. C. Larbalestier, Suppressed superconductivity on the surface of superconducting RF quality niobium for particle accelerating cavities, AIP Conf. Proc. **1352**, 142 (2011).

[6] A. A. Polyanskii, P. J. Lee, A. Gurevich, Zu-Hawn Sung, and D. C. Larbalestier, Magneto-optical study high-purity niobium for superconducting RF application, AIP Conf. Proc. **1352**, 186 (2011).

[7] C. Antoine, A. Aspart, S. Regnault, and A. Chincarini, Surface Studies: Method of Analysis and Results, *Proceeding of the 10th Workshop on RF Superconductivity, Tsukuba, Japan, 2001*, available online at https://accelconf.web.cern.ch/accelconf/srf01/papers/ma007.pdf; C. Z. Antoine, A. Aspart, M. Berthelot, Y. Gasser, J. P. Poupeau, and F. Valin, Morphological and Chemical studies of Nb Samples after Various Surface Treatment, *Proceeding of the 9th Workshop on RF Superconductivity, 1999*, available online at https://accelconf.web.cern.ch/accelconf/SRF99/papers/tup035.pdf.

[8] Z. H. Sung, P. J. Lee, and D. C. Larbalestier, Observation of the microstructure of grain boundary oxides in superconducting RF-quality niobium with high-resolution TEM (Transmission Electron Microscope), IEEE Trans. Appl. Supercond. **24**, 68 (2014).

[9] J. Halbritter, On Extrinsic - weak link - effects in the surface impedance of cuprate - and classical - superconductors, *Proceeding of the Fifth Workshop on RF Superconductivity, DESY, Hamburg, Germany, 1991*, available online at https://accelconf.web.cern.ch/accelconf/SRF91/papers/srf91g04.pdf.

[10] S.-C. Lee and S. M. Anlage, Study of local nonlinear properties using a near-field microwave microscope, IEEE Trans. Appl. Supercond. **13**, 3594 (2003).

[11] S.-C. Lee and S. M. Anlage, Spatially resolved nonlinearity measurements of $YBa_2Cu_3O_7$ bi-crystal grain boundaries, Appl. Phys. Lett. **82**, 1893 (2003).

[12] S.-C. Lee, S.-Y. Lee, and S. M. Anlage, Microwave nonlinearities of an isolated long $YBa_2Cu_3O_{7-\delta}$ bicrystal grain boundary, Phys. Rev. B **72**, 024527 (2005).

[13] D. I. Mircea and T. W. Clinton, Near-field microwave probe for local ferromagnetic resonance characterization, Appl. Phys. Lett. **90**, 142504 (2007).

[14] T. W. Clinton, N. Benatmane, J. Hohlfeld, and Erol Girt, Comparison of a near-field ferromagnetic resonance probe with pump-probe characterization of CoCrPt media, J. Appl. Phys. **103**, 07F546 (2008).

[15] G. Lamura, M. Aurino, A. Andreone, and J.-C. Villégier, First critical field measurements of superconducting films by third harmonic analysis, J. Appl. Phys. **106**, 053903 (2009).

[16] T. Takamasu, K. Sato, Y. Imanaka, and K. Takehana, Fabrication of a micro-coil pulsed magnet system and its application for solid state physics, J. Phys.: Conf. Ser. **51**, 591 (2006).

[17] K. Mackay, M. Bonfim, D. Givord, and A. Fontaine, 50 T pulsed magnetic fields in microcoils, J. Appl. Phys. **87**, 1996 (2000).

[18] N. Kikuchi, S. Okamoto, and O. Kitakami, Generation of nanosecond magnetic pulse field for switching experiments on a single Co/Pt nanodot, J. Appl. Phys. **105**, 07D506 (2009).

[19] Georg Woltersdorf and Christian H. Back, Microwave Assisted Switching of Single Domain $Ni_{80}Fe_{20}$ Elements, Phys. Rev. Lett. **99**, 227207 (2007).

[20] K. Yoshida, E. Uda, N. Udagawa, and Y. Kanai, Investigation on magnetic fields from field-generating layer in MAMR, IEEE Trans. Mag. **44**, 3408 (2008).

[21] D. Fang, H. Kurebayashi, J. Wunderlich, K. Výorný, L. P. Zârbo, R. P. Campion, A. Casiraghi, B. L. Gallagher, T. Jungwirth, and A. J. Ferguson1, Spin-orbit driven ferromagnetic resonance, Nat. Nanotechnol. **6**, 413 (2011).

[22] X. Zhu and J. G. Zhu, Bias-field-free microwave oscillator driven by perpendicularly polarized spin current, IEEE Trans. Magn. **42**, 2670 (2006).

[23] C. H. Sim, M. Moneck, T. Liew, and J. G. Zhu, Frequency-tunable perpendicular spin torque oscillator, J. Appl. Phys. **111**, 07C914 (2012).

[24] Tamin Tai, X. X. Xi, C. G. Zhuang, D. I. Mircea, and S. M. Anlage, Nonlinear near-field microwave microscope for RF defect localization in superconductors, IEEE Trans. Appl. Supercond. **21**, 2615 (2011).

[25] Tamin Tai, B. G. Ghamsari, T. Tan, C. G. Zhuang, X. X. Xi, and Steven M. Anlage, MgB_2 nonlinear properties investigated under localized high rf magnetic field excitation, Phys. Rev. ST Accel. Beams **15**, 122002 (2012).

[26] Tamin Tai, B. G. Ghamsari, and Steven M. Anlage, Nanoscale electrodynamic response of Nb superconductors, IEEE Trans. Appl. Supercond. **23**, 7100104 (2013).

[27] Tamin Tai, B. G. Ghamsari, and Steven M. Anlage, Modeling the nanoscale linear response of superconducting thin films measured by a scanning probe microwave microscope, J. Appl. Phys. **115**, 203908 (2014).

[28] Tamin Tai, Behnood G. Ghamsari, Thomas R. Bieler, Teng Tan, X. X. Xi, and Steven M. Anlage, Near-field microwave magnetic nanoscopy of superconducting radio frequency cavity materials, Appl. Phys. Lett. **104**, 232603 (2014).

[29] Tamin Tai, Behnood G. Ghamsari, J. H. Kang, S. Lee, C. B. Eom, and Steven M. Anlage, Localized high frequency electrodynamic behavior of optimally-doped $Ba(Fe_{1-x}Co_x)_2As_2$ single crystal films, arXiv:1507.03318.

[30] D. E. Oates, Y. D. Agassi, and B. H. Moeckly, Intermodulation distortion and nonlinearity in MgB_2: experiment and theory, IEEE Trans. Appl. Supercond. **17**, 2871 (2007).

[31] J. C. Booth, J. A. Beall, D. A. Rudman, L. R. Vale, and R. H. Ono, Geometry dependence of nonlinear effects in high temperature superconducting transmission lines at microwave frequencies, J. Appl. Phys. **86**, 1020 (1999).

[32] B. A. Willemsen, K. E. Kihlstrom, T. Dahm, D. J. Scalapino, B. Gowe, D. A. Bonn, and W. N. Hardy, Microwave loss and intermodulation in $Tl_2Ba_2CaCu_2O_y$ thin films, Phys. Rev. B **58**, 6650 (1998).

[33] Di Kang, Derek C. Baars, Thomas R. Bieler, and Chris C. Compton, Characterization of large grain Nb ingot microstructure using EBSP mapping and Laue camera methods, AIP Conf. Proc. **1352**, 90 (2011).

[34] Tamin Tai, Measuring electromagnetic properties of superconductors in high and localized RF magnetic field, Ph.D. thesis, University of Maryland-College Park, 2013, http://hdl.handle.net/1903/14668.

[35] Carson Jeffries, Q. H. Lam, Youngtae Kim, L. C. Bourne, and A. Zettl, Symmetry breaking and nonlinear electrodynamics in the ceramic superconductor $YBa_2Cu_3O_7$, Phys. Rev. B **37**, 9840 (1988).

[36] Ting-kang Xia and D. Stroud, Nonlinear electrodynamics and nonresonsnt microwave absoption in ceramic superconductors, Phys. Rev. B **39**, 4792 (1989).

[37] J. Halbitter, On the oxidation and on the superconductivity of niobium, Appl. Phys. A **43**, 1 (1987).

[38] G. Ciovati and J. Halbritter, Analysis of the medium field Q-slope in superconducting cavities made of bulk niobium, Phys. C: Supercond. **441**, 57 (2006).

[39] A. Gurevich and G. Ciovati, Dynamics of vortex penetration, jumpwise instabilities, and nonlinear surface resistance of type-II superconductors in strong rf fields, Phys. Rev. B **77**, 104501 (2008).

[40] Michael Tinkham, *Introduction to Superconductivity*, 2nd ed. (McGraw-Hill, New York, 1996).

[41] M. V. Milošević and F. M. Peeters, Vortex pinning in a superconducting film due to in-plane magnetized ferromagnets of different shapes: The London approximation, Phys. Rev. B **69**, 104522 (2004).

[42] A. V. Kapra, V. R. Misko, D. Y. Vodolazov, and F. M. Peeters, The guidance of vortex-antivortex pairs by in-plane magnetic dipoles in a superconducting finite-size film, Supercond. Sci. Technol. **24**, 024014 (2011).

[43] M. J. Van Bael, J. Bekaert, K. Temst, L. Van Look, M. V. Moshchalkov, Y. Bruynseraede, G. D. Howells, A. N. Grigorenko, and S. J. Bending, Local Observation of Field Polarity Dependent Flux Pinning by Magnetic Dipoles, Phys. Rev. Lett. **86**, 155 (2001).

[44] M. V. Milošević, S. V. Yampolskii, and F. M. Peeters, Magnetic pinning of vortices in a superconducting film: The antivortex magnetic dipole interaction energy in the London approximation, Phys. Rev. B **66**, 174519 (2002).

[45] V. Ambegaokar and A. Baratoff, Tunneling Between Superconductors, Phys. Rev. Lett. **10**, 486 (1963).

[46] J. R. Waldram, *Superconductivity of Metals and Cuprates* (IOP Publishing, Philadelphia, 1996), Chap. 10.

[47] J. Halbritter, Materials science and surface impedance Z (T, f, H) of Nb and YBCO and their quantitative modeling by the leakage current of weak links, Supercond. Sci. Technol. **12**, 883 (1999).

[48] Klaas B. Klaassen and Jack C. L. van Peppen, Nanosecond and sub-nanosecond writing experiments, IEEE Trans. Magn. **35**, 625 (1999).

[49] F. H. Liu, S. Shi, J. Wang, Y. Chen, K. Stoev, L. Leal, R. Saha, H. C. Tong, S. Dey, and M. Nojaba, Magnetic recording at a data rate of one gigabit per second, IEEE Trans. Magnetics **37**, 613 (2001).

[50] J. Halbritter, Granular superconductors and their intrinsic and extrinsic surface impedance, J. Supercond. **8**, 691 (1995).